MULTISCALE MODEL. SIMUL.
Vol. 14, No. 4, pp. 1301–1318

SEQUENTIAL HOMOGENIZATION OF REACTIVE TRANSPORT IN POLYDISPERSE POROUS MEDIA*

SVYATOSLAV KORNEEV† AND ILENIA BATTIATO†‡

Abstract. Direct numerical simulations of flow and transport in porous media are computationally prohibitive due to the disparity between the typical scale at which processes are well understood (e.g., the pore-scale) and the scale of interest (the system- or field-scale). Homogenization approaches overcome some of the difficulties of full pore-scale simulations by providing an upscaled representation of fine-scale processes. Real porous systems, e.g., rocks, pose additional challenges since they usually exhibit multimodal distributions in physical and chemical properties. Perforated domains, i.e., domains with impermeable inclusions embedded in a porous matrix, represent one such example. These hierarchical media cannot be approached by a single continuum formulation. Sequential homogenization techniques build a hierarchy of effective equations that sequentially carry the smallest scale information through the intermediate scales up to the macroscale. The advantage of sequential upscaling in handling multimodal distribution in physical and chemical properties lies in its computational efficiency compared to one-step homogenization: the information about smaller-scale heterogeneity is incorporated in the subsequent scales in terms of effective media properties. Yet, existence of one or multiple intermediate scales can significantly decrease the accuracy of multiscale formulations. We show that the accuracy of multiscale methods based on sequential upscaling is strongly influenced by a combination of geometric and dynamical scale separation conditions. In particular, we investigate under which conditions sequential homogenization of reactive solute transport in geometrically and chemically heterogeneous porous domains composed of bidisperse cylinders can accurately describe pore-scale processes. We show that under appropriate conditions, expressed in terms of Péclet and Damköhler numbers and a scales separation parameter, the sequential upscaling method has second-order accuracy. We compare sequential upscaling results with the direct solution of the fully resolved pore-scale problem.

Key words. perforated domains, sequential homogenization, heterogeneous porous media, upscaling, reactive transport

AMS subject classifications. 35B27, 76M50, 76F25

DOI. 10.1137/16M1074278

1. Introduction.

Direct numerical simulations of flow and transport in porous media with a complex hierarchy of scales can be computationally prohibitive, even for modern computational infrastructures. Since detailed physical models are usually well established at the smallest scale, while the scale of practical interest is often the largest one, direct simulations are practically impossible for systems with a wide span of spatial and temporal scales distribution. Multiscale methods [15, 23, 20, 6, and references therein] overcome these challenges by restricting the solution of the microscale problem to a subset of the entire domain, while across-scale coupling is ensured either numerically or analytically. Some examples of multiscale techniques include homogenization methods [18], multiscale finite element methods (MsFEMs) [14], generalized finite element methods (GFEMs) [9], and heterogeneous multiscale

*Received by the editors May 6, 2016; accepted for publication (in revised form) August 15, 2016; published electronically October 13, 2016.

http://www.siam.org/journals/mms/14-4/M107427.html

Funding: This work was funded by the U.S. Department of Energy (DOE), Office of Biological and Environmental Research, Subsurface Biogeochemical Research (SBR) Program through the SBR Scientific Focus Area at the Pacific Northwest National Laboratory.

†Department of Mechanical Engineering, San Diego State University, San Diego, CA 92182-1323 (skorneev@mail.sdsu.edu, ibattiato@mail.sdsu.edu).

‡Current address: Energy Resources Engineering Department, Stanford University, Stanford, CA 94305 (ibattiat@stanford.edu).

methods (HMMs) [20].

The key objective of any multiscale method of transport in porous media is to capture the macroscopic behavior of the solution by means of a localization approximation [20]. The latter allows one to determine effective (macroscopic) coefficients by solving a closure microscopic problem locally over a small computational domain. Two critical components of the closure problem are the size of the computational domain (here referred to as "unit cell") over which the microscale problem is solved (relative to the typical dimensionless size of heterogeneities ϵ) and the formulation of appropriate boundary conditions at the edges of the microscale domain. The scale separation parameter $\epsilon \ll 1$ is defined as the ratio between micro- and macroscopic characteristic length scales (or, alternatively, between the characteristic sizes of the microscopic structure and macroscopic domain). The homogenization limit exists if the upscaled solution converges to the averaged pore-scale solution as $\epsilon \to 0$. From a computational standpoint, it is generally preferable to reduce the size of the microscale problem to curb the computational costs associated with fine-scale resolution. Yet, this may be challenging or not possible altogether in porous media which exhibit heterogeneity on a multiplicity of scales due, e.g., to grain polydispersity. Many numerical studies have investigated how the accuracy of the continuum approximation is affected by both cell size and boundary conditions for any fixed scale separation parameter ϵ [34, 13, 7]. Alternatively, one could identify the conditions under which micro- and macroscale equations are decoupled; i.e., the closure problem solved on a unit cell is independent of macroscale quantities.

The condition $\epsilon \ll 1$ is generally considered sufficient to ensure that scales are well separated. This is the requirement common to many multiscale schemes. However, many studies have shown that additional dynamic conditions must be satisfied. In addition to geometrical constraints, the upscaling of advective-diffusive transport equations requires additional constraints on the magnitude of relevant dimensionless numbers. Micro- and macroscale transport become coupled at high Péclet numbers: this renders the upscaling difficult or even impossible [8]. Similar constraints are derived by Pavliotis [26] in the context of turbulent transport with mean flow. The author shows that upscaling is possible only when the strength of the mean flow is smaller than that of fluctuations. If the transport problem includes chemical reactions, the upscaling is complicated by strong cross-scale interactions between flow, diffusion, and reactions. Recently, it was shown that upscaling of such a problem requires additional conditions on the reactivity of the system [10, 11]. Neglecting such conditions undermines the accuracy of any numerical multiscale method.

Modeling of real heterogeneous porous systems, e.g., rocks, poses additional challenges since they usually exhibit multimodal distributions in physical and chemical properties. As a result, such hierarchical media cannot be approached by a single continuum formulation [29], and, generally, a nonlocal continuous dynamic arises [24, 28, 27]. Existence of one or multiple intermediate scales can significantly decrease the accuracy of multiscale formulations [23], except when fine scales possess a low energy spectrum [23]. Whenever the energy is distributed uniformly across multiple scales, two different approaches can be employed. The first approach consists in performing the expansion with respect to the smallest scale, while the entire domain is decomposed in mesoscale unit cells which include all microscale heterogeneities. This approach has very low computational efficiency for a highly heterogeneous system, since the closure problem (or the microscale problem) has to resolve all subgrid oscillations. We refer to this approach as single/one-step upscaling. The second method is referred to as sequential or reiterated homogenization [16, 22]. Sequential homog-

enization can be performed through sequential multiple-scale expansions. Sequential homogenization techniques build a hierarchy of effective equations that sequentially carry the smallest scale information through the intermediate scales up to the macroscale. The advantage of sequential upscaling relative to the one-step approach lies in its computational efficiency: a microscopic *homogeneous* domain is resolved for every relevant intermediate scale; the information about smaller-scale heterogeneity is incorporated in the subsequent scales in terms of effective media properties. Flow and transport in media with hierarchical heterogeneity has been thoroughly studied, particularly in the context of physically heterogeneous porous media, i.e., media with permeability contrast. Winter et al. advocate the use of sequential homogenization for heterogeneous composite (statistically inhomogeneous) media, albeit in the stochastic setting [31, 32, 33]. Differently from such classical works, we focus on the study of media that exhibit (statistically homogeneous) polydispersity (specifically bidispersity) at the pore-scale. One such example is given, e.g., by paraconglomerates, where impermeable pebbles are supported by fine grains which form a tight matrix. These systems are often referred to as "perforated" domains, i.e., domains with impermeable inclusions. Perforated domains differ from media with double/multiple (nonzero) permeability since the zero-permeability limit is singular [25], and alternative upscaling approaches from the pore- to the continuum-scale must be employed to obtain the effective properties of the medium. Sequential upscaling techniques represent a viable alternative to obtain transport coefficients at the macroscale. Lee and Engquist [21] proposed a sequential HMM to upscale advective-diffusive transport in shear flows with zero mean flow velocity. Sequential techniques were successfully developed for MsFEMs [20] and the method of homogenization [19] as well. Despite differences in their mathematical formulation, all these methods share the same requirement that scales must be geometrically separated, i.e., $\epsilon_i \ll 1$ for each couple $(i-1, i)$ of subsequent scales. Yet, the investigation of the dynamic conditions under which single- or multilevel homogenization can be performed has been generally overlooked, and an analysis of the impact of hierarchical pore-scale heterogeneity on homogenizability of nonlinear pore-scale phenomena is lacking.

We identify both geometric and dynamic conditions that guarantee scale separation and numerically study their impact on the upscaling approximation. We focus on two-scale perforated porous media, i.e., media with impermeable inclusions embedded inside a permeable matrix, with both physical (i.e., grain size distribution) and chemical (i.e., reaction rate coefficients) heterogeneity over two scales. In particular, we show that appropriate bounds on Damköhler and Peclét numbers need to be satisfied for the sequential upscaling to converge with second-order accuracy to one-step homogenization. These findings highlight the importance of satisfying appropriate dynamic conditions, in addtion to the more classical geometric scale separation condition, to preserve the accuracy of any numerical multiscale scheme.

In section 2 we start with the problem formulation and define the geometry of the domain, the pore-scale flow and transport equations, as well as their dimensionless formulation. In section 3, we discuss the single-step and sequential homogenization approaches and identify the applicability conditions sufficient to guarantee that the two-step upscaled equation represents the one-step homogenized model with second-order accuracy. In section 4, we perform numerical simulations of the flow and transport closure problems in both one- and two-step homogenization. We show that the sequential homogenization provides sufficient accuracy when the length scales are well separated, and specific constraints on the dimensionless Damköhler and Peclét numbers are met. To verify the latter, we perform full pore-scale transport simulations for

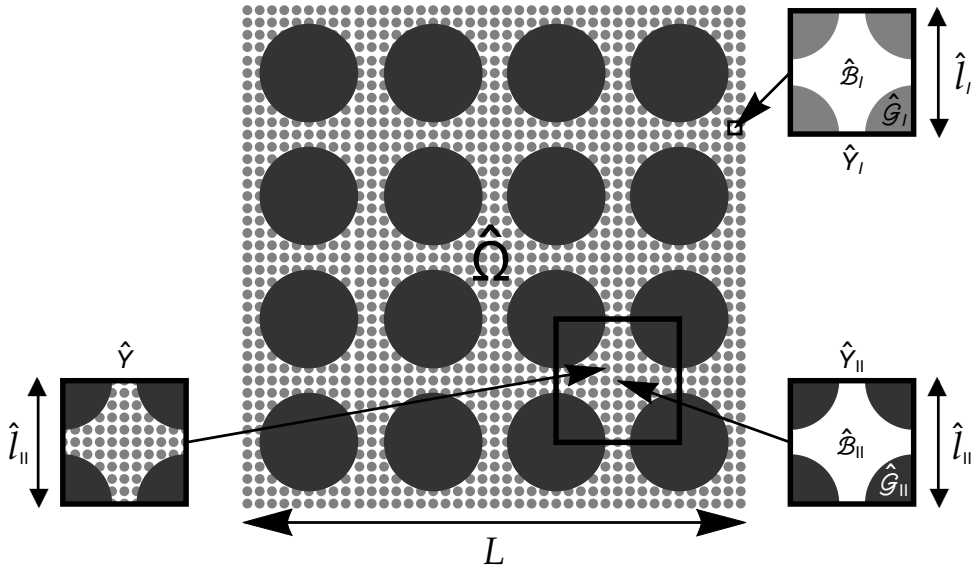

FIG. 1. *Schematic representation of a bidisperse porous medium composed of arrays of micro- and mesoscale cylinders with different surface reactivities. The figure shows the full domain and the unit cells at each scale.*

different values of Damköhler and Peclét numbers. In section 5 we finalize the results from previous sections.

2. Problem formulation.

2.1. Geometry. Consider a two-dimensional (2D) heterogeneous porous domain $\hat{\Omega}$ made of a periodic array of bisized impermeable cylinders (see Figure 1). While we choose a 2D geometry as an illustrative example, extensions to three dimensions are straightforward. The domain can be decomposed in two subdomains $\hat{\Omega}_{\rm I}$ and $\hat{\Omega}_{\rm II}$ with characteristic length scales $\hat{l}_{\rm I}$ and $\hat{l}_{\rm II}$, respectively, such that $\hat{\Omega} = \hat{\Omega}_{\rm I} \cup \hat{\Omega}_{\rm II}$ and $\hat{l}_{\rm I} \ll \hat{l}_{\rm II} \ll L$, where L is the size of $\hat{\Omega}$. We will refer to scales $\hat{l}_{\rm I}$ and $\hat{l}_{\rm II}$ as the micro- and the mesoscale, respectively.

The domain $\hat{\Omega}$ is obtained as a collection of repeating unit cells $\hat{Y} = \hat{\mathcal{B}} \cup \hat{\mathcal{G}}$, where $\hat{\mathcal{B}}$ is the pore space and $\hat{\mathcal{G}}$ the solid obstacles. They are separated by the smooth surface $\hat{\Gamma} = \hat{\Sigma}_{\rm I} \cup \hat{\Sigma}_{\rm II}$, where $\hat{\Sigma}_{\rm I}$ and $\hat{\Sigma}_{\rm II}$ are the total surface area of the microscale and mesoscale cylinders, respectively. The total pore-space $\hat{\mathcal{B}}^\epsilon = \bigcup \hat{\mathcal{B}}$ forms a multiconnected pore-space domain bounded by the smooth surface $\hat{\Gamma}^\epsilon = \hat{\Sigma}^\epsilon_{\rm I} \cup \hat{\Sigma}^\epsilon_{\rm II}$. Similarly, the subdomains $\hat{\Omega}_{\rm I}$ and $\hat{\Omega}_{\rm II}$ can be decomposed in a collection of spatially periodic unit cells $\hat{Y}_{\rm I} = \hat{\mathcal{B}}_{\rm I} \cup \hat{\mathcal{G}}_{\rm I}$ and $\hat{Y}_{\rm II} = \hat{\mathcal{B}}_{\rm II} \cup \hat{\mathcal{G}}_{\rm II}$, where $\hat{\mathcal{B}}_{\rm I}$ and $\hat{\mathcal{B}}_{\rm II}$ are the pore space, and $\hat{\mathcal{G}}_{\rm I}$ and $\hat{\mathcal{G}}_{\rm II}$ are the solid obstacles separated by the smooth surfaces $\hat{\Gamma}_{\rm I}$ and $\hat{\Gamma}_{\rm II}$, respectively.

2.2. Pore-scale governing equations. The pore-space $\hat{\mathcal{B}}^\epsilon$ is fully saturated with an incompressible fluid with dynamic viscosity $\hat{\nu}$. Its steady state flow at low Reynolds number is governed by the Stokes equations subject to the no-slip boundary condition on the solid-liquid interfaces,

$$\hat{\nu}\hat{\nabla}^2\hat{\mathbf{v}} - \hat{\nabla}\hat{p} = 0, \quad \hat{\nabla}\cdot\hat{\mathbf{v}} = 0, \quad \hat{\mathbf{x}} \in \hat{\mathcal{B}}^\epsilon, \quad \hat{\mathbf{v}} = 0, \quad \hat{\mathbf{x}} \in \hat{\Gamma}^\epsilon, \tag{1}$$

with $\hat{\mathbf{v}}(\hat{\mathbf{x}})$ the fluid velocity and $\hat{p}$ the dynamic pressure. The concentration of a dissolved solute undergoing a heterogeneous nonlinear reaction on the liquid-solid interface $\hat{\Gamma}^\epsilon$ obeys an advection-diffusion equation

$$\frac{\partial \hat{c}}{\partial t} + \hat{\mathbf{v}} \cdot \hat{\nabla} \hat{c} = \hat{\nabla} \cdot (\hat{\mathbf{D}} \hat{\nabla} \hat{c}), \quad \hat{\mathbf{x}} \in \hat{\mathcal{B}}^\epsilon, \tag{2}$$

subject to [10, eq. (4)]

$$-\mathbf{n} \cdot \hat{\mathbf{D}} \hat{\nabla} \hat{c} = \hat{k}_{\mathrm{I}} \left(\hat{c}^a - \bar{c}^a \right), \quad \hat{\mathbf{x}} \in \hat{\Sigma}^\epsilon_{\mathrm{I}}, \tag{3}$$

$$-\mathbf{n} \cdot \hat{\mathbf{D}} \hat{\nabla} \hat{c} = \hat{k}_{\mathrm{II}} \left(\hat{c}^a - \bar{c}^a \right), \quad \hat{\mathbf{x}} \in \hat{\Sigma}^\epsilon_{\mathrm{II}}, \tag{4}$$

where $\hat{\mathbf{D}}$ is molecular diffusion, $\hat{k}_{\mathrm{I}}$ and $\hat{k}_{\mathrm{II}}$ are the reaction rates on the surface of the micro- and mesoscale obstacles, respectively, and $\bar{c}^a$ is an equilibrium concentration.

2.3. Dimensionless formulation. Let us introduce the dimensionless variables

$$c = \frac{\hat{c}}{\bar{c}}, \quad \mathbf{x} = \frac{\hat{\mathbf{x}}}{L}, \quad \mathbf{v} = \frac{\hat{\mathbf{v}}}{U}, \quad \mathbf{D} = \frac{\hat{\mathbf{D}}}{D}, \quad p = \frac{\hat{p} \hat{l}_{\mathrm{I}}^2}{\hat{\nu} U L}, \tag{5}$$

where D and U are characteristic values of pore-scale diffusion and flow velocity. Here, the pressure term is scaled so as to balance the viscous term at the pore-scale [22]. We define four time scales associated with diffusion ($\hat{t}_D$), advection ($\hat{t}_A$), and reaction on the micro- and mesoscales I and II ($\hat{t}_{R_{\mathrm{I}}}$ and $\hat{t}_{R_{\mathrm{II}}}$),

$$\hat{t}_D = \frac{L^2}{D}, \quad \hat{t}_A = \frac{L}{U}, \quad \hat{t}_{R_{\mathrm{I}}} = \frac{L}{\hat{k}_{\mathrm{I}} \bar{c}^{a-1}}, \quad \hat{t}_{R_{\mathrm{II}}} = \frac{L}{\hat{k}_{\mathrm{II}} \bar{c}^{a-1}}. \tag{6}$$

Ratios between these time scales define the dimensionless Damköhler ($\mathrm{Da}_{\mathrm{I}} = \hat{t}_D / \hat{t}_{R_{\mathrm{I}}}$ and $\mathrm{Da}_{\mathrm{II}} = \hat{t}_D / \hat{t}_{R_{\mathrm{II}}}$) and Péclet $\left(\mathrm{Pe} = \hat{t}_D / \hat{t}_A\right)$ numbers,

$$\mathrm{Da}_{\mathrm{I}} = \frac{L \hat{k}_{\mathrm{I}} \bar{c}^{a-1}}{D}, \quad \mathrm{Da}_{\mathrm{II}} = \frac{L \hat{k}_{\mathrm{II}} \bar{c}^{a-1}}{D}, \quad \text{and} \quad \mathrm{Pe} = \frac{UL}{D}. \tag{7}$$

Also, we define the separation of scale parameters

$$\epsilon_{\mathrm{I}} = \frac{\hat{l}_{\mathrm{I}}}{L} \quad \text{and} \quad \epsilon_{\mathrm{II}} = \frac{\hat{l}_{\mathrm{II}}}{L} \tag{8}$$

with $\epsilon_{\mathrm{I}} < \epsilon_{\mathrm{II}} \ll 1$. Using (5) and scaling time with $\hat{t}_A$, the flow and transport equations (1)–(4) can be cast in dimensionless form

$$\epsilon_{\mathrm{I}}^2 \nabla^2 \mathbf{v} - \nabla p = 0, \quad \nabla \cdot \mathbf{v} = 0, \quad \mathbf{x} \in \mathcal{B}^\epsilon, \quad \mathbf{v} = 0, \quad \mathbf{x} \in \Gamma^\epsilon, \tag{9}$$

and

$$\frac{\partial c}{\partial t} + \nabla \cdot (-\mathbf{D} \nabla c + \mathrm{Pe} \mathbf{v} c) = 0, \quad \mathbf{x} \in \mathcal{B}^\epsilon, \tag{10}$$

subject to

$$\begin{aligned} -\mathbf{n} \cdot \mathbf{D} \nabla c &= \mathrm{Da}_{\mathrm{I}} \left(c^a - 1 \right), \quad \mathbf{x} \in \Sigma^\epsilon_{\mathrm{I}}, \\ -\mathbf{n} \cdot \mathbf{D} \nabla c &= \mathrm{Da}_{\mathrm{II}} \left(c^a - 1 \right), \quad \mathbf{x} \in \Sigma^\epsilon_{\mathrm{II}}. \end{aligned} \tag{11}$$

In the following section, the upscaling of the pore-scale equations (9)–(11) is presented.

3. Homogenization. Homogenization aims to derive effective equations for pore-scale state variables averaged over a representative volume or unit cell. The homogenized (macroscale) equation is obtained by expanding pore-scale quantities in power series in terms of a perturbation parameter. The derivation of homogenized equations for systems with heterogeneity on two scales $\epsilon_{\rm I}$ and $\epsilon_{\rm II}$ can be conducted in one or two steps.

In one-step homogenization, the domain is decomposed in repeating unit cells Y of size $\epsilon_{\rm II}$ constituted of micro- and mesoscale cylinders (see Figure 1). The local averages of a pore-scale quantity $\mathcal{A}(\mathbf{x},t)$ are defined as

$$\langle\mathcal{A}\rangle \equiv \frac{1}{|\mathcal{B}|_{\mathbf{y}_{\rm I}}}\int_{\mathcal{B}(\mathbf{x})}\mathcal{A}\mathrm{d}\mathbf{y}_{\rm I} \quad \text{and} \quad \langle\mathcal{A}\rangle_{\Gamma} \equiv \frac{1}{|\Gamma|_{\mathbf{y}_{\rm I}}}\int_{\Gamma(\mathbf{x})}\mathcal{A}\mathrm{d}\mathbf{y}_{\rm I}, \tag{12}$$

where $\mathbf{y}_{\rm I} = \mathbf{x}/\epsilon_{\rm I} \in \mathcal{B}(\mathbf{x})$ is a fast space variable, $|\mathcal{B}|_{\mathbf{y}_{\rm I}}$ is the pore-space volume of Y normalized by $\mathbf{y}_{\rm I}$, and $|\Gamma|_{\mathbf{y}_{\rm I}}$ is the rescaled surface of the liquid-solid boundaries in the unit cell. Furthermore, the pore-scale quantities are represented as $\mathcal{A}(\mathbf{x},t) \longrightarrow \mathcal{A}(\mathbf{x},\mathbf{y}_{\rm I},t)$ and approximated by the asymptotic series

$$\mathcal{A}(\mathbf{x},\mathbf{y}_{\rm I},t) = \sum_{m=0}^{\infty}\epsilon_{\rm I}^{m}\mathcal{A}_m(\mathbf{x},\mathbf{y}_{\rm I},t), \tag{13}$$

where $\mathcal{A}_m(\mathbf{x},\mathbf{y}_{\rm I},t)$ are Y-periodic in $\mathbf{y}_{\rm I}$.

The continuum-scale model describes the pore-scale dynamics with an accuracy defined by the truncation error of the power series rather than by the averaging procedure over the unit cell.

The method of sequential homogenization consists of forward iterations of one-step homogenization from the smallest scale $\epsilon_{\rm I}$ to the largest scale $\epsilon_{\rm II}$. The unit cells for the first and second homogenization steps are $Y_{\rm I}$ and $Y_{\rm II}$, respectively. The local averages on each scale are defined as

$$\langle\mathcal{A}\rangle_{\rm I} \equiv \frac{1}{|\mathcal{B}_{\rm I}|_{\mathbf{y}_{\rm I}}}\int_{\mathcal{B}_{\rm I}(\mathbf{x})}\mathcal{A}\mathrm{d}\mathbf{y}_{\rm I} \quad \text{and} \quad \langle\mathcal{A}\rangle_{\Gamma_{\rm I}} \equiv \frac{1}{|\Gamma_{\rm I}|_{\mathbf{y}_{\rm I}}}\int_{\Gamma_{\rm I}(\mathbf{x})}\mathcal{A}\mathrm{d}\mathbf{y}_{\rm I}, \tag{14}$$

$$\langle\mathcal{A}\rangle_{\rm II} \equiv \frac{1}{|\mathcal{B}_{\rm II}|_{\mathbf{y}_{\rm II}}}\int_{\mathcal{B}_{\rm II}(\mathbf{x})}\mathcal{A}\mathrm{d}\mathbf{y}_{\rm II} \quad \text{and} \quad \langle\mathcal{A}\rangle_{\Gamma_{\rm II}} \equiv \frac{1}{|\Gamma_{\rm II}|_{\mathbf{y}_{\rm II}}}\int_{\Gamma_{\rm II}(\mathbf{x})}\mathcal{A}\mathrm{d}\mathbf{y}_{\rm I}, \tag{15}$$

where $\mathbf{y}_{\rm I} = \mathbf{x}/\epsilon_{\rm I} \in \mathcal{B}_{\rm I}(\mathbf{x})$ and $\mathbf{y}_{\rm II} = \mathbf{x}/\epsilon_{\rm II} \in \mathcal{B}_{\rm II}(\mathbf{x})$ are the fast variables. Here, $|\mathcal{B}_{\rm I}|_{\mathbf{y}_{\rm I}}$ and $|\mathcal{B}_{\rm II}|_{\mathbf{y}_{\rm II}}$ are the rescaled pore-space volumes, and $|\Gamma_{\rm I}|_{\mathbf{y}_{\rm I}}$, and $|\Gamma_{\rm II}|_{\mathbf{y}_{\rm II}}$ are the rescaled surface of the solid-liquid interfaces $\Gamma_{\rm I}$ and $\Gamma_{\rm II}$ in $Y_{\rm I}$ and $Y_{\rm II}$, respectively. Variables at each scale are represented as follows:

$$\mathcal{A}_{\rm I}(\mathbf{x},\mathbf{y}_{\rm I},t) = \sum_{m=0}^{\infty}\epsilon_{\rm I}^{m}\mathcal{A}_{m,{\rm I}}(\mathbf{x},\mathbf{y}_{\rm I},t), \tag{16}$$

$$\mathcal{A}_{\rm II}(\mathbf{x},\mathbf{y}_{\rm II},t) = \sum_{m=0}^{\infty}\epsilon_{\rm II}^{m}\mathcal{A}_{m,{\rm II}}(\mathbf{x},\mathbf{y}_{\rm II},t), \tag{17}$$

where $\mathcal{A}$ is a dummy variable.

Compared to one-step homogenization, sequential homogenization is less accurate since, in addition to the truncation error, it introduces a new error related to the quasi-periodicity of porous matrix at scale $\epsilon_{\rm I}$, where periodicity breaks down at the boundary of the mesoscale obstacles (see Figure 2). In the following section we present the upscaling results of one- and two-step homogenization.

3.1. One-step homogenization. The upscaling of the Stokes equations (9) from the pore-scale to the continuum-scale has been widely studied [8, 17, 19, and references therein]. These studies demonstrated that, for porous media with constant porosity, Darcy's law and the continuity equations for the averaged flow velocity

$$\langle \mathbf{v}_0 \rangle = -\mathbf{K} \cdot \nabla_{\mathbf{x}} p_0, \quad \nabla \cdot \langle \mathbf{v}_0 \rangle = 0, \quad \mathbf{x} \in \Omega, \tag{18}$$

provide an effective representation of Stokes equations. In (18), $\mathbf{v}_0$ and p_0 are the leading order terms in the expansion (13) for the pore-scale velocity and pressure, $\mathbf{K} = \langle \mathbf{k}(\mathbf{y}_{\text{I}}) \rangle$ is the permeability tensor, and $\mathbf{k}(\mathbf{y}_{\text{I}})$ is a closure variable. The latter is defined as the solution of the following closure problem:

$$\nabla^2_{\mathbf{y}_{\text{I}}} \mathbf{k} + \mathbf{I} - \nabla_{\mathbf{y}_{\text{I}}} \mathbf{a} = 0, \quad \nabla_{\mathbf{y}_{\text{I}}} \cdot \mathbf{k} = 0, \quad \mathbf{y}_{\text{I}} \in \mathcal{B}, \tag{19}$$

subject to nonslip boundary condition $\mathbf{k}(\mathbf{y}_{\text{I}}) = 0$ for $\mathbf{y}_{\text{I}} \in \Gamma$. The vector $\mathbf{a}$ is a Y-periodic function and satisfies the condition $\langle \mathbf{a} \rangle = 0$.

Spatially homogeneous reaction rates. Before discussing the upscaling of the reactive transport equations for a porous medium with chemically heterogeneous obstacles, we present results for the homogeneous case. This will be used as a reference to derive the applicability conditions of continuum-scale models for transport with spatially heterogeneous reaction rates.

The homogenization of the pore-scale reactive transport equations (10)–(11) where $\text{Da}_{\text{I}} = \text{Da}_{\text{II}} = \text{Da}$ leads to an effective advection-dispersion-reaction equation (ADRE) that approximates pore-scale transport with second order accuracy $\mathcal{O}\left(\epsilon_{\text{I}}^2\right)$

$$\frac{\partial \langle \tilde{c} \rangle}{\partial t} = \nabla \cdot \left(\mathbf{D}^\star \nabla \langle \tilde{c} \rangle - \text{Pe} \langle \tilde{c} \rangle \langle \tilde{\mathbf{v}} \rangle \right) - \text{Da} \mathcal{K}^\star \left(\langle \tilde{c} \rangle^a - 1 \right), \quad \mathbf{x} \in \Omega, \tag{20}$$

provided the following constraints are met [10]:

1. $\epsilon_{\text{I}} \ll 1$,
2. $\text{Pe} < \epsilon_{\text{I}}^{-2}$,
3. $\text{Da}/\text{Pe} < \epsilon_{\text{I}}$,
4. $\text{Da} < 1$.

Constraint 1 is the classical scale-separation condition, and constraints 2, 3, and 4 guarantee that the system is well mixed at the pore-scale. In (20), $\langle \tilde{c} \rangle = \langle c_0 \rangle + \epsilon_{\text{I}} \langle c_1 \rangle$ and $\langle \tilde{\mathbf{v}} \rangle = \langle \mathbf{v}_0 \rangle + \epsilon_{\text{I}} \langle \mathbf{v}_1 \rangle$ are the first-order expansions of the pore-scale concentration and flow velocity. The averaged flow velocity $\langle \tilde{\mathbf{v}} \rangle$ can be calculated as a solution of Darcy's equation (18). The truncation error of (18) is zero for a periodic domain, i.e., $\mathbf{v} = \mathbf{v}_0 = \tilde{\mathbf{v}}$. Further, $\mathcal{K}^\star$ is the effective reaction rate constant defined as

$$\mathcal{K}^\star = \frac{|\Gamma|_{\mathbf{y}_{\text{I}}}}{\epsilon_{\text{I}} |\mathcal{B}|_{\mathbf{y}_{\text{I}}}}, \tag{21}$$

and $\mathbf{D}^\star$ is the dispersion tensor given by

$$\mathbf{D}^\star = \langle \mathbf{D} (\mathbf{I} + \nabla_{\mathbf{y}_{\text{I}}} \boldsymbol{\chi}) \rangle + \epsilon_{\text{I}} \text{Pe} \langle \mathbf{v} \otimes \boldsymbol{\chi} \rangle. \tag{22}$$

The closure variable $\boldsymbol{\chi}(\mathbf{y}_{\text{I}})$ has zero mean, $\langle \boldsymbol{\chi}(\mathbf{y}_{\text{I}}) \rangle = 0$, and it is defined as the solution of the local problem

$$-\nabla_{\mathbf{y}_{\text{I}}} \cdot \left[\mathbf{D} \left(\nabla_{\mathbf{y}_{\text{I}}} \boldsymbol{\chi} + \mathbf{I} \right) \right] + \epsilon_{\text{I}} \text{Pe} \mathbf{v} \nabla_{\mathbf{y}_{\text{I}}} \boldsymbol{\chi} = \epsilon_{\text{I}} \text{Pe} \left(\langle \mathbf{v} \rangle - \mathbf{v} \right), \quad \mathbf{y}_{\text{I}} \in \mathcal{B}, \tag{23}$$

subject to

$$\mathbf{n} \cdot \mathbf{D} \left(\nabla_{\mathbf{y}_{\text{I}}} \boldsymbol{\chi} + \mathbf{I} \right) = 0, \quad \mathbf{y}_{\text{I}} \in \Gamma, \tag{24}$$

where $\mathbf{v} = -\mathbf{k} \cdot \nabla_{\mathbf{x}} p_0$ and p_0 is a solution of Darcy's equation (18).

Spatially heterogeneous reaction rates. The upscaling of the transport equation in the presence of spatially heterogeneous reaction rates is technically similar to that of chemically homogeneous porous media. Let us define Pe and Da numbers in terms of ϵ_{I} and ϵ_{II}:

$$\text{Pe} = \epsilon_{\text{I}}^{\alpha_{\text{I}}} = \epsilon_{\text{II}}^{\alpha_{\text{II}}}, \quad \text{Da}_{\text{I}} = \epsilon_{\text{I}}^{\beta_{\text{I}}}, \quad \text{Da}_{\text{II}} = \epsilon_{\text{II}}^{\beta_{\text{II}}}. \tag{25}$$

We also introduce the ratio between length scales

$$\epsilon_{\text{I}} = \epsilon_{\text{II}}^{\gamma}, \tag{26}$$

where γ defines the separation of length scales. Here, we give just a sketch of the derivation (see [10] for technical details related the chemically homogeneous case). The effective reaction term is given as the surface integral $\mathcal{R}$ with respect to $\mathbf{y}_{\text{I}}$ of the pore-scale reaction term over the total boundary $\Gamma = \Sigma_{\text{I}} \cup \Sigma_{\text{II}}$ normalized by the total volume of the cell's empty space $|\mathcal{B}|_{\mathbf{y}_{\text{I}}}$,

$$\begin{aligned}\mathcal{R} &= \frac{1}{|\mathcal{B}|_{\mathbf{y}_{\text{I}}}} \int_{\Sigma_{\text{I}}} \text{Da}_{\text{I}}(1 - c_0^a) \mathrm{d}\mathbf{y}_{\text{I}} + \frac{1}{|\mathcal{B}|_{\mathbf{y}_{\text{I}}}} \int_{\Sigma_{\text{II}}} \text{Da}_{\text{II}}(1 - c_0^a) \mathrm{d}\mathbf{y}_{\text{I}} \\ &= (1 - \langle c_0 \rangle^a) \left(\frac{|\Sigma_{\text{I}}|_{\mathbf{y}_{\text{I}}}}{|\mathcal{B}|_{\mathbf{y}_{\text{I}}}} \text{Da}_{\text{I}} + \frac{|\Sigma_{\text{II}}|_{\mathbf{y}_{\text{I}}}}{|\mathcal{B}|_{\mathbf{y}_{\text{I}}}} \text{Da}_{\text{II}} \right),\end{aligned} \tag{27}$$

where $|\Sigma_{\text{I}}|_{\mathbf{y}_{\text{I}}}$ and $|\Sigma_{\text{II}}|_{\mathbf{y}_{\text{I}}}$ are the total surface of pore- and mesoscale obstacles, respectively. Cell volume and surface areas scale as

$$|\Sigma_{\text{I}}|_{\mathbf{y}_{\text{I}}} = |\Gamma_{\text{I}}|_{\mathbf{y}_{\text{I}}} \frac{|\mathcal{B}|_{\mathbf{y}_{\text{I}}}}{|\mathcal{B}_{\text{I}}|_{\mathbf{y}_{\text{I}}}}, \quad |\Sigma_{\text{II}}|_{\mathbf{y}_{\text{I}}} \approx \frac{\epsilon_{\text{II}}}{\epsilon_{\text{I}}} |\Gamma_{\text{II}}|_{\mathbf{y}_{\text{II}}} \frac{|\mathcal{B}|_{\mathbf{y}_{\text{II}}}}{|\mathcal{B}_{\text{II}}|_{\mathbf{y}_{\text{II}}}}, \quad |\mathcal{B}|_{\mathbf{y}_{\text{I}}} = \left(\frac{\epsilon_{\text{II}}}{\epsilon_{\text{I}}} \right)^2 |\mathcal{B}|_{\mathbf{y}_{\text{II}}}, \tag{28}$$

where $|\mathcal{B}|_{\mathbf{y}_{\text{I}}} / |\mathcal{B}_{\text{I}}|_{\mathbf{y}_{\text{I}}}$ is the number of the microscale unit cells inside the mesoscale unit cell and $|\mathcal{B}|_{\mathbf{y}_{\text{II}}} / |\mathcal{B}_{\text{II}}|_{\mathbf{y}_{\text{II}}}$ is the porosity of the porous matrix.

Combining (28) with (27) leads to

$$\mathcal{R} \approx (1 - \langle c_0 \rangle^a) \left(\frac{|\Gamma_{\text{I}}|_{\mathbf{y}_{\text{I}}}}{|\mathcal{B}_{\text{I}}|_{\mathbf{y}_{\text{I}}}} \text{Da}_{\text{I}} + \frac{\epsilon_{\text{I}}}{\epsilon_{\text{II}}} \frac{|\Gamma_{\text{II}}|_{\mathbf{y}_{\text{II}}}}{|\mathcal{B}_{\text{II}}|_{\mathbf{y}_{\text{II}}}} \text{Da}_{\text{II}} \right). \tag{29}$$

Finally, (29) is divided by ϵ_{I}, and the effective equation takes the form

$$\frac{\partial \langle \tilde{c} \rangle}{\partial t} = \nabla \cdot (\mathbf{D}^\star \nabla \langle \tilde{c} \rangle - \text{Pe} \langle \tilde{c} \rangle \langle \mathbf{v} \rangle) - (\text{Da}_{\text{I}} \mathcal{K}_{\text{I}}^\star + \text{Da}_{\text{II}} \mathcal{K}_{\text{II}}^\star) (\langle \tilde{c} \rangle^a - 1), \quad \mathbf{x} \in \Omega, \tag{30}$$

where

$$\mathcal{K}_{\text{I}}^\star = \frac{|\Gamma_{\text{I}}|_{\mathbf{y}_{\text{I}}}}{\epsilon_{\text{I}} |\mathcal{B}_{\text{I}}|_{\mathbf{y}_{\text{I}}}} \quad \text{and} \quad \mathcal{K}_{\text{II}}^\star = \frac{|\Gamma_{\text{II}}|_{\mathbf{y}_{\text{II}}}}{\epsilon_{\text{II}} |\mathcal{B}_{\text{II}}|_{\mathbf{y}_{\text{II}}}}. \tag{31}$$

In order to ensure that scales are well separated, i.e., that the solution of the local problem is independent from the global field, additional conditions on the order of magnitude of both Damköhler and Peclét numbers need to be satisfied. Specifically,

$$\text{Pe} < \epsilon_{\text{I}}^{-2} \quad \text{and} \quad \text{Pe} < \epsilon_{\text{II}}^{-2}, \tag{32}$$

$$\text{Da}_{\text{I}}/\text{Pe} < \epsilon_{\text{I}} \quad \text{and} \quad \text{Da}_{\text{II}}/\text{Pe} < \epsilon_{\text{II}}, \tag{33}$$

and

$$\mathrm{Da}_{\mathrm{I}} < 1 \quad \text{and} \quad \mathrm{Da}_{\mathrm{II}} < 1, \tag{34}$$

where the first two sets of inequalities provide constraints on separation of the local problem (23) from the global dynamic, while the second set ensures that global field quantities do not affect the boundary conditions of the local problem (24). All these conditions have to be satisfied concurrently.

3.2. Sequential homogenization. Sequential homogenization consists in applying homogenization over scales I and II sequentially. As a result, the upscaled equations obtained from sequential homogenization represent an approximation of the macroscale equations determined from single-step homogenization. Here, we provide the main results of sequential homogenization for flow and heterogeneous reactive transport. An example of the rigorous procedure is provided in [22].

The first step consists in upscaling flow and transport at scale I, i.e., over the unit cell Y_{I}. The upscaling of flow over Y_{I} leads to Darcy's equation, i.e.,

$$\langle \mathbf{v} \rangle_{\mathrm{I}} = -\mathbf{K}_{\mathrm{I}} \cdot \nabla_{\mathbf{x}} p_0, \quad \nabla \cdot \langle \mathbf{v} \rangle_{\mathrm{I}} = 0, \quad \mathbf{x} \in \Omega_{\mathrm{I}}, \quad \mathbf{n} \cdot \langle \mathbf{v} \rangle_{\mathrm{I}} = 0, \quad \mathbf{x} \in \Gamma_{\mathrm{II}}, \tag{35}$$

where $\mathbf{K}_{\mathrm{I}} = \langle \mathbf{k}_{\mathrm{I}} (\mathbf{y}_{\mathrm{I}}) \rangle_{\mathrm{I}}$ is the permeability tensor and the local problem is defined as

$$\nabla^2_{\mathbf{y}_{\mathrm{I}}} \mathbf{k}_{\mathrm{I}} + \mathbf{I} - \nabla_{\mathbf{y}_{\mathrm{I}}} \mathbf{a}_{\mathrm{I}} = 0, \quad \nabla_{\mathbf{y}_{\mathrm{I}}} \cdot \mathbf{k}_{\mathrm{I}} = 0, \tag{36}$$

subject to

$$\mathbf{y}_{\mathrm{I}} \in \mathcal{B}_{\mathrm{I}}, \quad \mathbf{k}_{\mathrm{I}} = 0, \quad \mathbf{y}_{\mathrm{I}} \in \Gamma_{\mathrm{I}}. \tag{37}$$

The transport equation after the first step takes the form

$$\frac{\partial \langle \tilde{c} \rangle_{\mathrm{I}}}{\partial t} = \nabla \cdot (\mathbf{D}^{\star}_{\mathrm{I}} \nabla \langle \tilde{c} \rangle_{\mathrm{I}} - \mathrm{Pe} \langle \tilde{c} \rangle_{\mathrm{I}} \langle \mathbf{v} \rangle_{\mathrm{I}}) - \mathrm{Da}_{\mathrm{I}} \mathcal{K}^{\star}_{\mathrm{I}} (\langle \tilde{c} \rangle^{a}_{\mathrm{I}} - 1), \quad \mathbf{x} \in \Omega_{\mathrm{II}}, \tag{38}$$

subject to

$$-\mathbf{n} \cdot \mathbf{D}^{\star}_{\mathrm{I}} \nabla \langle \tilde{c} \rangle_{\mathrm{I}} = \mathrm{Da}_{\mathrm{II}} (\langle \tilde{c} \rangle^{a}_{\mathrm{I}} - 1), \quad \mathbf{x} \in \Gamma_{\mathrm{II}}, \tag{39}$$

where $\langle \tilde{c} \rangle_{\mathrm{I}} = \langle c_{0,\mathrm{I}} \rangle_{\mathrm{I}} + \epsilon_{\mathrm{I}} \langle c_{1,\mathrm{I}} \rangle_{\mathrm{I}}$ and $\mathbf{D}^{\star}_{\mathrm{I}}$ and $\mathcal{K}^{\star}_{\mathrm{I}}$ are defined by

$$\mathbf{D}^{\star}_{\mathrm{I}} = \langle \mathbf{D} (\mathbf{I} + \nabla_{\mathbf{y}_{\mathrm{I}}} \boldsymbol{\chi}_{\mathrm{I}}) \rangle_{\mathrm{I}} + \epsilon_{\mathrm{I}} \mathrm{Pe} \langle \mathbf{v}_{\mathrm{I}} \otimes \boldsymbol{\chi}_{\mathrm{I}} \rangle_{\mathrm{I}} \tag{40}$$

and (31), respectively. The closure variable $\boldsymbol{\chi}_{\mathrm{I}}$ is defined by the solution of the local problem

$$-\nabla_{\mathbf{y}_{\mathrm{I}}} \cdot [\mathbf{D} (\nabla_{\mathbf{y}_{\mathrm{I}}} \boldsymbol{\chi}_{\mathrm{I}} + \mathbf{I})] + \epsilon_{\mathrm{I}} \mathrm{Pe} \mathbf{v}_{\mathrm{I}} \nabla_{\mathbf{y}_{\mathrm{I}}} \boldsymbol{\chi}_{\mathrm{I}} = \epsilon_{\mathrm{I}} \mathrm{Pe} (\langle \mathbf{v}_{\mathrm{I}} \rangle_{\mathrm{I}} - \mathbf{v}_{\mathrm{I}}), \quad \mathbf{y}_{\mathrm{I}} \in \mathcal{B}_{\mathrm{I}}, \tag{41}$$

subject to

$$\mathbf{n} \cdot \mathbf{D} (\nabla_{\mathbf{y}_{\mathrm{I}}} \boldsymbol{\chi}_{\mathrm{I}} + \mathbf{I}) = 0, \quad \mathbf{y}_{\mathrm{I}} \in \Gamma_{\mathrm{II}}, \tag{42}$$

where $\mathbf{v}_{\mathrm{I}} = -\mathbf{k}_{\mathrm{I}} \cdot \nabla_{\mathbf{x}} p_0$ is a solution of the local problem (36). In the following step, homogenization is performed for the Darcy flow past the mesoscale obstacles Ω_{II} over the unit cell Y_{II}. After the second homogenization step, Darcy's equation takes the form

$$\langle \mathbf{v} \rangle_{\mathrm{II}} = -\mathbf{K}_{\mathrm{II}} \cdot \nabla_{\mathbf{x}} p_0, \quad \nabla \cdot \langle \mathbf{v} \rangle_{\mathrm{II}} = 0, \quad \mathbf{x} \in \Omega, \tag{43}$$

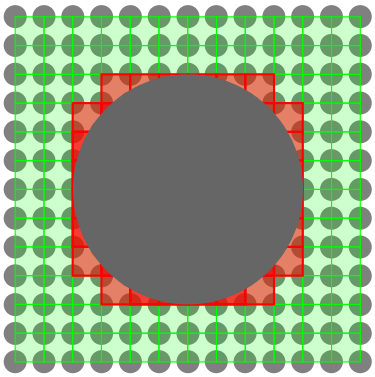

FIG. 2. *Schematic representation of two types of pore-scale unit cells. Green cells are quasi-periodic cells, where the closure problem is solved, while red cells are nonperiodic cells, where the periodicity of the porous matrix breaks down.*

where $\mathbf{K}_{\text{II}} = \langle \mathbf{K}_{\text{I}} \left(\nabla_{\mathbf{y}_{\text{II}}} \mathbf{k}_{\text{II}} \left(\mathbf{y}_{\text{II}} \right) + \mathbf{I} \right) \rangle_{\text{II}}$ is the "renormalized" permeability tensor, defined by the local problem

$$- \nabla_{\mathbf{y}_{\text{II}}} \cdot \left[\mathbf{K}_{\text{I}} \left(\nabla_{\mathbf{y}_{\text{II}}} \mathbf{k}_{\text{II}} + \mathbf{I} \right) \right] = 0, \tag{44}$$

subject to

$$\mathbf{n} \cdot \mathbf{K}_{\text{I}} \left(\nabla_{\mathbf{y}_{\text{II}}} \mathbf{k}_{\text{II}} + \mathbf{I} \right) = 0, \quad \mathbf{y}_{\text{II}} \in \Gamma_{\text{II}}. \tag{45}$$

The effective transport equation is

$$\frac{\partial \langle \tilde{c} \rangle_{\text{II}}}{\partial t} = \nabla \cdot (\mathbf{D}^{\star}_{\text{II}} \nabla \langle \tilde{c} \rangle_{\text{II}} - \text{Pe} \langle \tilde{c} \rangle_{\text{II}} \langle \mathbf{v} \rangle_{\text{II}}) - (\text{Da}_{\text{I}} \mathcal{K}^{\star}_{\text{I}} + \text{Da}_{\text{II}} \mathcal{K}^{\star}_{\text{II}}) \left(\langle \tilde{c} \rangle^{a}_{\text{II}} - 1 \right), \quad \mathbf{x} \in \Omega, \tag{46}$$

where $\langle \tilde{c} \rangle_{\text{II}} = \langle c_{0,\text{II}} \rangle_{\text{II}} + \epsilon_{\text{II}} \langle c_{1,\text{II}} \rangle_{\text{II}}$, and $\mathcal{K}^{\star}_{\text{II}}$ is given by (31). The dispersion tensors and $\mathbf{D}^{\star}_{\text{II}}$ are

$$\mathbf{D}^{\star}_{\text{II}} = \langle \mathbf{D}^{\star}_{\text{I}} \left(\mathbf{I} + \nabla_{\mathbf{y}_{\text{II}}} \boldsymbol{\chi}_{\text{II}} \right) \rangle_{\text{II}} + \epsilon_{\text{II}} \text{Pe} \langle \mathbf{v}_{\text{II}} \otimes \boldsymbol{\chi}_{\text{II}} \rangle_{\text{II}}, \tag{47}$$

where $\mathbf{v}_{\text{II}} = -\mathbf{k}_{\text{II}} \cdot \nabla_{\mathbf{x}} p_0$ and the closure variable $\boldsymbol{\chi}_{\text{II}}$ is defined as the solution of the closure problem over the unit cell Y_{II},

$$-\nabla_{\mathbf{y}_{\text{II}}} \cdot \left[\mathbf{D}^{\star}_{\text{I}} \left(\nabla_{\mathbf{y}_{\text{II}}} \boldsymbol{\chi}_{\text{II}} + \mathbf{I} \right) \right] + \epsilon_{\text{II}} \text{Pe} \mathbf{v}_{\text{II}} \nabla_{\mathbf{y}_{\text{II}}} \boldsymbol{\chi}_{\text{II}} = \epsilon_{\text{II}} \text{Pe} \left(\langle \mathbf{v}_{\text{II}} \rangle_{\text{II}} - \mathbf{v}_{\text{II}} \right), \quad \mathbf{y}_{\text{II}} \in \mathcal{B}_{\text{II}}, \tag{48}$$

subject to

$$\mathbf{n} \cdot \mathbf{D}^{\star}_{\text{I}} \left(\nabla_{\mathbf{y}_{\text{II}}} \boldsymbol{\chi}_{\text{II}} + \mathbf{I} \right) = 0, \quad \mathbf{y}_{\text{II}} \in \Gamma_{\text{II}}. \tag{49}$$

The accuracy of (46) is $\mathcal{O}(\epsilon^2_{\text{II}})$ provided the applicability conditions are met at every upscaling step. These conditions are discussed in section 3.2.1. It is worth noticing that while the derivation is only formal, it can be numerically verified a posteriori, as shown in section 4.

3.2.1. Applicability condition for sequential homogenization. The applicability conditions of any given homogenized model define the range of dimensionless parameters that guarantee that the macroscale model describes fine-scale processes

with a prescribed accuracy (generally second-order in the separation of scale parameter). While such applicability conditions were originally derived for single-step homogenization in terms of bounds on Da and Pe numbers [10, 11], they can be easily extended to sequential homogenization, since all such constraints must be sequentially satisfied at each upscaling step.

In addition to constraints on geometric scale separation between the pore-scale and the macroscale (i.e., $\epsilon_{\text{I}} \ll 1$), and the mesoscale and the macroscale (i.e., $\epsilon_{\text{II}} \ll 1$), an appropriate scale separation between scales I and II must be satisfied; i.e., an additional condition, expressed in terms of the exponent γ, exists. Such a condition accounts for the additional error in sequential homogenization originating from the quasi-periodicity of the porous matrix Ω, where the nonperiodic unit cells are located at the boundary of mesoscale obstacles (see Figure 2). The error associated to lack of periodicity $\mathcal{E}_{np}$ scales with the number N_{np} of nonperiodic unit cells on the boundary of the mesoscale objects, where $N_{np} \sim \epsilon_{\text{I}}/\epsilon_{\text{II}}$, i.e.,

$$\mathcal{E}_{np} \sim \frac{\epsilon_{\text{I}}}{\epsilon_{\text{II}}}. \tag{50}$$

The requirement that such an error be less than the truncation error of the effective transport equation (46) $\mathcal{E} = \mathcal{O}(\epsilon_{\text{II}}^2)$ leads to the condition

$$\mathcal{E}_{np} \lesssim \mathcal{E} \quad \text{or} \quad \frac{\epsilon_{\text{I}}}{\epsilon_{\text{II}}} \lesssim \epsilon_{\text{II}}^2, \tag{51}$$

which is satisfied if

$$\gamma \gtrsim 3. \tag{52}$$

Condition (52) also decouples pore-scale dispersion from mesoscale advection. If $\text{Pe} < 1/\epsilon_{\text{I}}$, the second term in (40) and (41) and the RHS of (41) become negligible; i.e., transport at scale I is mainly diffusive, and dispersion at scale I is decoupled from advection at scale II . This condition is always met since $\text{Pe} < 1/\epsilon_{\text{II}}^2 < 1/\epsilon_{\text{I}}$ when (52) is satisfied.

In the following section we numerically verify the condition (52) by direct comparison between sequential and one-step solution of the closure problem for a range of $\epsilon_{\text{I}}/\epsilon_{\text{II}}$ values. Conditions (32)–(34) are verified by comparing full pore-scale simulations with the solution of the homogenized equation.

4. Numerical validation. To verify the applicability conditions of sequential homogenization, we perform a series of 2D numerical experiments. In the first set of numerical simulations (section 4.1), we analyze the convergence rate of the sequential closure problem to the one-step closure problem for different values of the ratio $\epsilon_{\text{I}}/\epsilon_{\text{II}}$.

In section 4.2, we verify the applicability conditions for the Da and Pe numbers by comparing the fully resolved pore-scale problem with the upscaled model.

All simulations are run with the free open-source computational fluid dynamics code OpenFOAM [5]. To optimize the simulations time, we consider flow and transport through a porous medium Ω_c composed of a single array of periodic unit cells Y_c (see Figure 3). We impose the nonslip and nonpenetration boundary conditions on the top and bottom of the domain Ω_c, and inlet and outlet boundary conditions on the left and right boundaries, respectively. The ratio between the obstacle diameter and the unit cell side is set to 0.3, and the resolution of the pore-scale unit cell is set to 60×60 finite volume cells. The parameter a in the reactive boundary conditions (11) is set to 1.

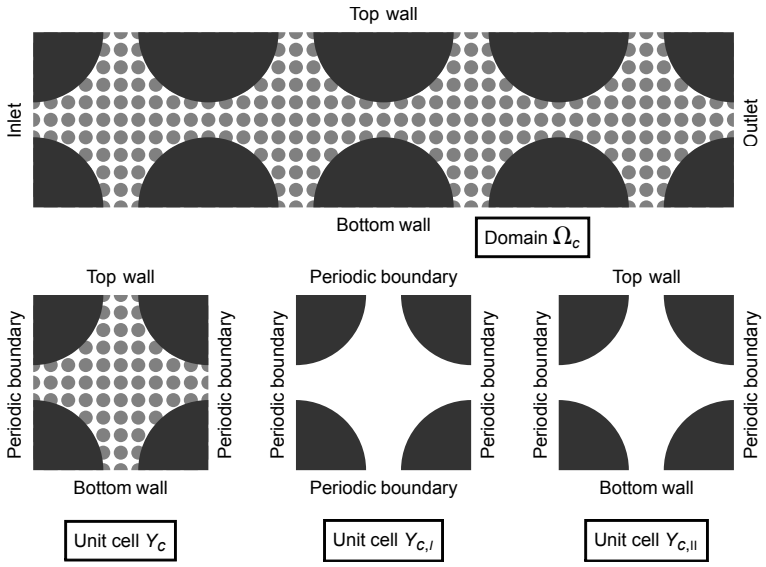

FIG. 3. *Schematic representation of the computational domain and unit cells: (Top) entire computational domain Ω_c; (Bottom) unit cell Y_c (left), unit cell $Y_{c,I}$ (middle), and unit cell $Y_{c,II}$ (right).*

Boundary conditions on the right and left boundaries of the periodic unit cells Y_c, $Y_{c,\mathrm{I}}$, and $Y_{c,\mathrm{II}}$ at each scale (pore-scale, scale I, and scale II, respectively) are periodic. The top and bottom boundaries of $Y_{c,\mathrm{I}}$ and $Y_{c,\mathrm{II}}$ are periodic and no-slip/no-penetration, respectively (see Figure 3).

4.1. Geometric scales separation condition $\gamma \gtrsim 3$. In order to test the geometric scale separation condition $\gamma \gtrsim 3$ and its impact on the accuracy of the sequential homogenization approximation, we solve both the one-step ((19), (23), and (24)) and sequential closure problems ((36) and (44) for permeability, and (41) and (48) for the dispersion coefficient).

We consider different length scale ratios $\mathrm{N_I} = \epsilon_{\mathrm{II}}/\epsilon_{\mathrm{I}}$, with $\mathrm{N_I} = \{20, 25, 30, 40, 50, 60\}$ and $\gamma = 3$; see (26). We then estimate the relative error between the sequential and one-step solutions. We solve the closure problems for $\mathrm{Pe} = 0$ and $\mathrm{Pe} = 15$ corresponding to diffusion- and advection-dominated transport regimes, respectively. To check the robustness of the solution, we use both low and high order finite volume methods. The relative errors between permeability and dispersion coefficient obtained from sequential and one-step homogenization for each scenario and for both high and low order schemes are plotted in Figure 4. As predicted in the analysis presented in section 3.2.1, the error is always bounded by the curve ϵ_{II}^2 when $\gamma = 3$ and is always greater than ϵ_{II}^2 when $\gamma = 2$. It is worth noticing that the truncation error of the second step of sequential homogenization is on the order of $\mathcal{O}\left(\epsilon_{\mathrm{II}}^2\right)$. The error boundedness supports the assumption that the leading-order error is inversely proportional to the number of nonperiodic cells along the obstacles' geometrical boundary and that such an error is of the same order of magnitude as the truncation error of the asymptotic expansion when $\gamma = 3$.

In Figure 5 we plot the solutions for the closure problem of the one-step homogenization (left) and the second step of sequential homogenization (right). The solution

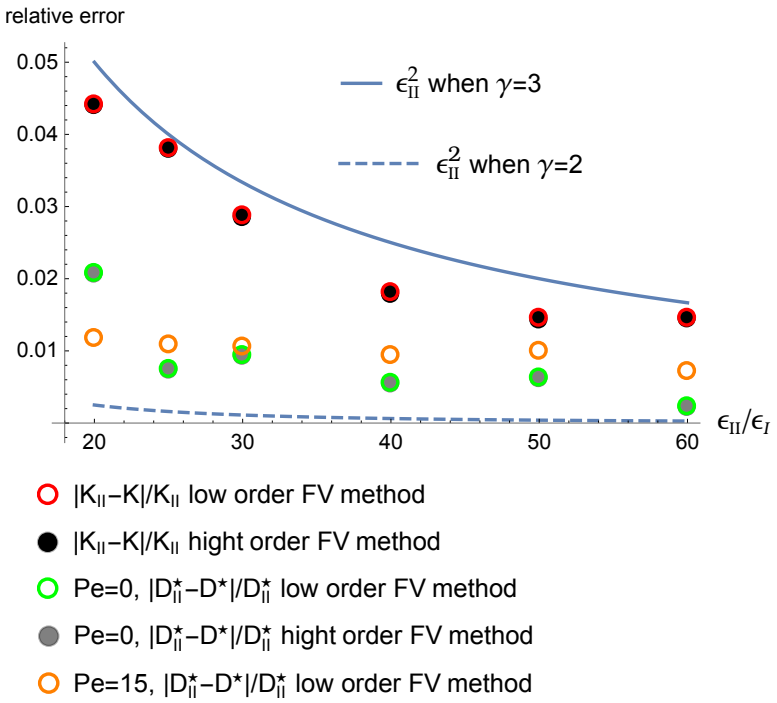

FIG. 4. *Relative error between the dispersion coefficient* $|D^\star_{II} - D^\star| / D^\star$ *(green, grey, and orange symbols) and the permeability tensor* $|K_{II} - K| / K_{II}$ *(red and black symbols) calculated from sequential and one-step homogenization for different values of* (i) *the length scale ratio* ϵ_{II}/ϵ_I, (ii) *the order of the finite volume scheme (i.e., second and fourth), and* (iii) *the values of Peclét number (i.e.,* $Pe = 0$ *and* $Pe = 15$*). Here,* K_{II} *and* K *are the* xx*-components of the permeability tensor obtained from sequential homogenization (at scale* II*) and one-step homogenization, respectively. Similarly,* $D^\star_{II}$ *and* $D^\star$ *are the* xx*-components of the dispersion tensor from sequential homogenization (at scale* II*) and one-step homogenization, respectively. The solid and dashed lines represent the curve* ϵ^2_{II} *when* $\gamma = 3$ *and* $\gamma = 2$*, respectively; see* (26)*. The circles and discs correspond to second- and fourth-order finite volume discretization schemes, respectively.*

of the sequential closure problem is the homogenization limit of the closure problem in one-step homogenization.

The main advantage of sequential homogenization over one-step homogenization is in the computational speedup and efficiency. For example, the computational grid in one-step homogenization can be as much as three orders of magnitude larger compared to the sequential homogenization requirements.

4.2. Dynamic conditions on Damköhler and Peclét numbers. To verify the applicability conditions on Peclét and Damköhler numbers, we perform steady-state pore-scale transport simulations. We consider four scenarios whose characteristic parameters are summarized in Table 1.

The presence of heterogeneity raises the challenge of how to define an appropriate Peclét number (or characteristic velocity) upon which the bounds (32)–(34) are based. A priori there are multiple equivalent ways to define the characteristic velocity (or Peclét number) in a heterogeneous system. For example, it could be selected as, e.g., the mode, the median, or the mean value of the flow velocity distribution. The latter should be sufficiently narrow to be defined by one characteristic value.

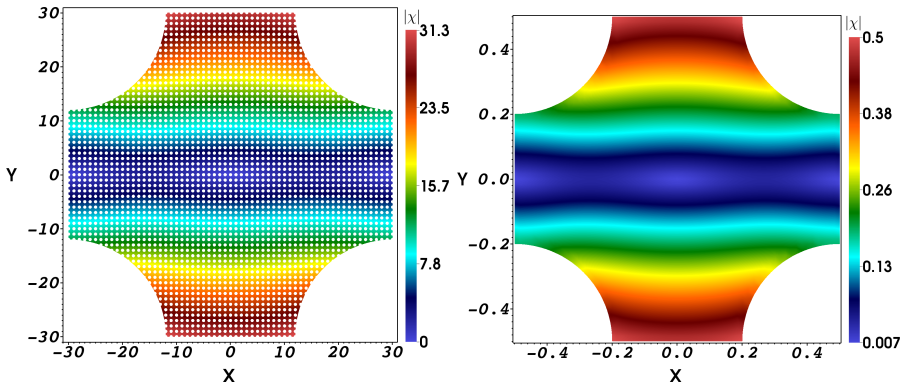

FIG. 5. *Spatial distribution of the closure variable, solution of the local problem for the transport equation with* $Pe = 0$ *and* $\epsilon_{II}/\epsilon_I = 60$*, in the unit cell* Y_c *rescaled to* $\mathbf{y}_I$ *of the one-step closure problem (left), and unit cell* $Y_{c,II}$ *rescaled to* $\mathbf{y}_{II}$ *of the sequential closure problem (at scale II) (right).*

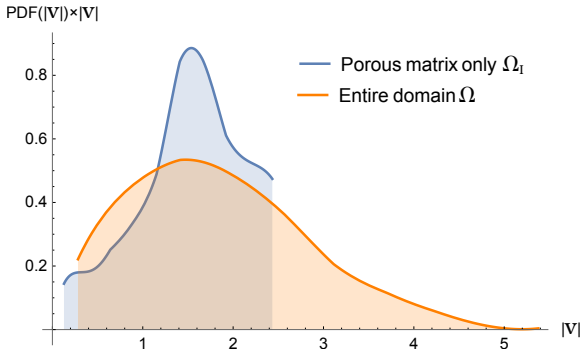

FIG. 6. *Weighted probability density function (wPDF) of the flow velocity. The wPDF is weighted by the mass flux, where fluid density is set to* 1*. The wPDF is obtained from the solution of the Stokes equation* (10) *either in the porous matrix* Ω_I *(blue line) or in the entire domain* Ω *(orange line). In both cases, the* x*-component of the average flow velocity is* 1*.*

In Figure 6, we determine the velocity distribution weighted by the mass flux, or the weighted probability density function (wPDF) [12] $\mathrm{PDF}(|v|) \times |v|$, for both the full bidisperse domain Ω and the monodisperse porous matrix Ω_{I}. As apparent from Figure 6, the span of the wPDF for the bidisperse domain is wider than that for the porous matrix. Yet, it is narrow enough to be described by a single characteristic value. Finally, we choose the characteristic velocity to calculate the Peclét number by setting to 1 the average flow velocity along the horizontal axis of the computational domain Ω_c. The global pressure gradient $\nabla_x p_0$ is determined as $\nabla_x p_0 = 1/K$ where K is the permeability.

In Figure 8, we show a comparison between the solution of the effective ADRE (46) and the first-order reconstruction of the averaged pore-scale concentration, where Cases 1 and 3 correspond to scenarios where the applicability conditions on dimensionless numbers on each scale are met, while Cases 2 and 4 violate such conditions at scale I and II, respectively. For each scenario, we estimate the relative error of sequential homogenization, where the error is defined as the maximum difference between the first-order reconstruction of the cell averaged pore-scale solution and the upscaled solution (see Table 1).

TABLE 1

Parameter values for different test cases with $\epsilon_I = 0.008$, $\epsilon_{II} = 0.2$, $\gamma = 3$, *and* $\epsilon_{II}^2 = 0.04$. *In the table,* $\langle c \rangle$ *is the first-order reconstruction of the* Y_c *cell averaged pore-scale solution and* $\langle \tilde{c} \rangle_{II}$ *is the solution of* (46). *The dispersion tensor in* (46) *is calculated by sequential homogenization.*

Case	$\mathrm{Da_I}$	$\mathrm{Da_{II}}$	Pe	$\max\left[\left(\langle c\rangle - \langle \tilde{c}\rangle_{\mathrm{II}}\right) / \langle c\rangle\right]$	ϵ_{II}^2
1	0.05	0.5	15	0.027	0.04
2	0.3	0.5	15	0.099	0.04
3	0.001	0.1	1	0.021	0.04
4	0.001	2.0	1	0.080	0.04

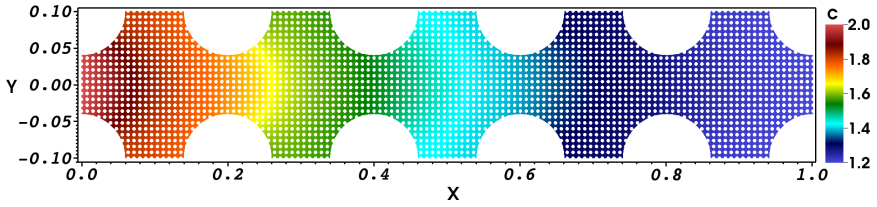

FIG. 7. *Steady-state pore-scale concentration profile for Case* 1 *of Table* 1.

Since the numerical averaging of the pore-scale solution over a unit cell is a zero-order approximation, we use a finite volumes (FV) first-order conservative total variation diminishing (TVD) reconstruction scheme in order to capture the second-order accuracy necessary to quantify the upscaling error. The conservative property of the scheme uniquely defines the position of the cell center (red dots in Figure (8)), while the TVD property uniquely defines the total slope of the reconstructed solution (orange line in Figure (8)), where the total variation of the reconstructed solution is equal to the total variation of the upscaled solution.

The results are summarized in Table 1. As predicted by our theoretical analysis, the error for Cases 1 and 3 is always bounded by ϵ_{II}^2, unlike for Cases 2 and 4, which do not satisfy conditions (32)–(34). Figure 7 shows the example of the steady-state pore-scale concentration distribution.

4.3. Technical details. All numerical simulations are run in OpenFOAM. The mesh is prepared with *snappyHexMesh*, with standard sets of parameters [4]. Both the Stokes equation (9) and the flow closure problem (19) and (36) are solved by *simpleFoam*, with zero convection and an additional external constant forcing, respectively. In sequential homogenization, the local flow problem for scale II (44) is solved through *laplacianFoam*. The pore-scale transport equation (10) and local problems (23), (41), and (48) are solved with *scalarTransportFoam*. For the low and high order simulations we use first- and fourth-order spatial schemes, respectively, [2]. The discretized equations were solved by standard linear solvers [3]. Boundary conditions (11), (24), (39), (45), and (49) were implemented through the extension *groovyBC* of the OpenFOAM library *swak4Foam* [30]. We run OpenFOAM in parallel on Amazon Web Services (AWS) compute-optimized EC2 36 core instance [1].

5. Conclusions. Sequential homogenization is a powerful approach to curbing computational costs associated with upscaling of physically and chemically heterogeneous porous media. In this work, we focus on bidisperse porous media, and as an illustrative example we consider a 2D domain composed of arrays of micro- and mesoscale cylinders of dimensionless size $\epsilon_{\mathrm{I}} \ll 1$ and $\epsilon_{\mathrm{II}} \ll 1$ with $\epsilon_{\mathrm{I}} \ll \epsilon_{\mathrm{II}}$, respectively. We show that conditions on geometric scale separation, i.e., $\epsilon_{\mathrm{I}} \lesssim \epsilon_{\mathrm{II}}^3$, and on

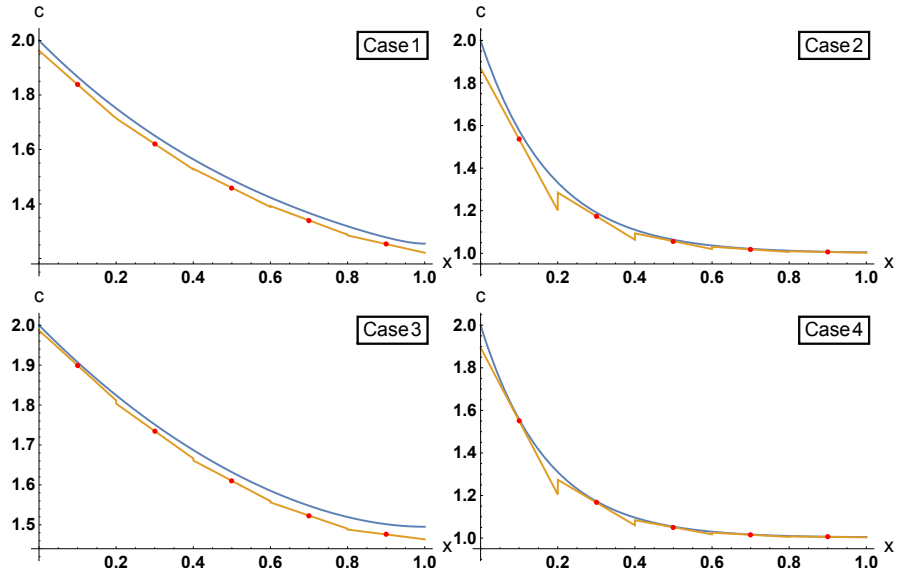

FIG. 8. *Comparison between the first-order reconstruction of the averaged pore-scale steady-state concentration over the unit cell Y_c (orange line) and the average concentration obtained as a solution of the ADRE* (46) *(blue line) for Cases* 1, 2, 3, *and* 4 *of Table* 1. *The red dots show the position of the center of the cell Y_c as determined by the TVD scheme.*

the order of magnitude of Damköhler and Peclét numbers, i.e., constraints (32)–(34), must be met for the sequentially homogenized problem to converge with prescribed accuracy to the upscaled solution. Such conditions guarantee that (i) the error due to lack of periodicity in proximity of the mesoscale cylinders is bounded by the truncation error of the asymptotic expansion, and (ii) the system is well mixed on both the microscale and the mesoscale. We test the aforementioned conditions numerically by comparing the solution of the closure problems in one-step and sequential homogenization methods with full pore-scale simulations of reactive transport past arrays of bisized cylinders with heterogeneous reaction rates. The numerical simulations, run in OpenFOAM, confirm that the conditions on scale separation and Damköhler and Peclét numbers are sufficient to guarantee that the sequentially homogenized solution represents pore-scale processes within errors of order ϵ_{II}^2. These results highlight that simple requirements on the length ratio between micro- and macroscales, e.g., $\epsilon_{\text{I}} \ll 1$ and $\epsilon_{\text{II}} \ll 1$, are not sufficient to guarantee that the upscaled system accurately represents pore-scale processes. Also, the applicability conditions in sequential homogenization can be useful in the development of multiscale methods for reactive transport in heterogeneous porous media.

Acknowledgments. We thank A. M. Tartakovsky and T. D. Scheibe for the useful discussions, and the OpenFOAM community for the development of a powerful simulation platform. We are also very grateful to Amazon AWS Programs for Research and Education for providing us with the computational time at their cloud infrastructure.

REFERENCES

[1] *Amazon Web Services*, https://aws.amazon.com/.

[2] *OpenFOAM User Guide:* 4.4 *Numerical Schemes*, http://cfd.direct/openfoam/user-guide/fvschemes/.
[3] *OpenFOAM User Guide:* 4.5 *Solution and Algorithm Control*, http://cfd.direct/openfoam/user-guide/fvsolution/.
[4] *OpenFOAM User Guide:* 5.4 *Mesh Generation, SnappyHexMesh*, http://cfd.direct/openfoam/user-guide/snappyhexmesh/.
[5] *The OpenFOAM Foundation*, http://www.openfoam.org/.
[6] J. E. Aarnes and Y. Efendiev, *An adaptive multiscale method for simulation of fluid flow in heterogeneous porous media*, Multiscale Model. Simul., 5 (2006), pp. 918–939, https://doi.org/10.1137/050645117.
[7] B. Amaziane, A. Bourgeat, and M. Jurak, *Effective macrodiffusion in solute transport through heterogeneous porous media*, Multiscale Model. Simul., 5 (2006), pp. 184–204, https://doi.org/10.1137/050630490.
[8] J. Auriault and P. Adler, *Taylor dispersion in porous media: Analysis by multiple scale expansions*, Adv. Water Res., 18 (1995), pp. 217–226, https://doi.org/10.1016/0309-1708(95)00011-7.
[9] I. Babuška, U. Banerjee, and J. E. Osborn, *Generalized finite element methods—main ideas, results and perspective*, Internat. J. Comput. Methods, 1 (2004), pp. 67–103, https://doi.org/10.1142/S0219876204000083.
[10] I. Battiato and D. M. Tartakovsky, *Applicability regimes for macroscopic models of reactive transport in porous media*, J. Contaminant Hydrol., 120–121 (2011), pp. 18–26, https://doi.org/10.1016/j.jconhyd.2010.05.005.
[11] F. Boso and I. Battiato, *Homogenizability conditions for multicomponent reactive transport*, Adv. Water Res., 62 (2013), pp. 254–265, https://doi.org/10.1016/j.advwatres.2013.07.014.
[12] F. Cherblanc, A. Ahmadi, and M. Quintard, *Two-domain description of solute transport in heterogeneous porous media: Comparison between theoretical predictions and numerical experiments*, Adv. Water Res., 30 (2007), pp. 1127–1143, https://doi.org/10.1016/j.advwatres.2006.10.004.
[13] L. J. Durlovsky, *Numerical calculation of equivalent grid block permeability tensors for heterogeneous porous media*, Water Resour. Res., 27 (1991), pp. 699–708, https://doi.org/10.1029/91WR00107.
[14] Y. Efendiev and T. Hou, *Multiscale finite element methods for porous media flows and their applications*, Appl. Numer. Math., 57 (2007), pp. 577–596, https://doi.org/10.1016/j.apnum.2006.07.009.
[15] V. L. Hauge, *Multiscale Methods and Flow-based Gridding for Flow and Transport in Porous Media*, Ph.D. thesis, Norwegian University of Science and Technology, Trondheim, Norway, 2010.
[16] A. Holmbom, N. Svanstedt, and N. Wellander, *Multiscale convergence and reiterated homogenization of parabolic problems*, Appl. Math., 50 (2005), pp. 131–151, https://doi.org/10.1007/s10492-005-0009-z.
[17] M. H. Holmes, *Introduction to Perturbation Methods*, Texts Appl. Math. 20, Springer, New York, 1995.
[18] U. Hornung, *Applications of the homogenization method to flow and transport in porous media*, in Summer School on Flow and Transport in Porous Media (Beijing, China, 1988), World Scientific, Singapore, 1992, pp. 167–222.
[19] U. Hornung, *Homogenization and Porous Media*, Interdisciplinary Applied Mathematics, Springer-Verlag, New York, 1997.
[20] T. Y. Hou and Y. Efendiev, *Multiscale Finite Element Methods*, Springer, New York, 2009, https://doi.org/10.1007/978-0-387-09496-0.
[21] Y. Lee and B. Engquist, *Multiscale Numerical Methods for Passive Advection-Diffusion in Incompressible Turbulent Flow Fields*, preprint, arXiv:1510.00451 [math.NA], 2015.
[22] C. C. Mei and J.-L. Auriault, *Mechanics of heterogeneous porous media with several spatial scales*, Proc. Roy. Soc. London Ser. A, 426 (1989), pp. 391–423, https://doi.org/10.1098/rspa.1989.0132.
[23] P. Ming and X. Yue, *Numerical methods for multiscale elliptic problems*, J. Comput. Phys., 214 (2006), pp. 421–445, https://doi.org/10.1016/j.jcp.2005.09.024.
[24] S. P. Neuman and D. M. Tartakovsky, *Perspective on theories of non-Fickian transport in heterogeneous media*, Adv. Water Res., 32 (2009), pp. 670–680, https://doi.org/10.1016/j.advwatres.2008.08.005.
[25] M. Panfilov, *Macroscale Models of Flow through Highly Heterogeneous Porous Media*, Theory and Applications of Transport in Porous Media 16, Springer, Dordrecht, The Netherlands, 2000, https://doi.org/10.1007/978-94-015-9582-7.

[26] G. A. Pavliotis, *Homogenization Theory for Advection-Diffusion Equations with Mean Flow*, Ph.D. thesis, Rensselaer Polytechnic Institute, Troy, NY, 2002.

[27] G. Severino, A. Santini, and V. M. Monetti, *Modelling water flow and solute transport in heterogeneous unsaturated porous media*, in Advances in Modeling Agricultural Systems, Springer Optim. Appl. 25, Springer, New York, 2009, pp. 361–383, https://doi.org/10.1007/978-0-387-75181-8_17.

[28] G. Severino, D. M. Tartakovsky, G. Srinivasan, and H. Viswanathan, *Lagrangian models of reactive transport in heterogeneous porous media with uncertain properties*, Proc. R. Soc. Lond. Ser. A Math. Phys. Eng. Sci., 468 (2011), pp. 1154–1174, https://doi.org/10.1098/rspa.2011.0375.

[29] C. Steefel, D. DePaolo, and P. Lichtner, *Reactive transport modeling: An essential tool and a new research approach for the Earth sciences*, Earth Planetary Sci. Lett., 240 (2005), pp. 539–558, https://doi.org/10.1016/j.epsl.2005.09.017.

[30] R. Vilums, *Implementation of transient Robin boundary conditions in OpenFOAM*, in Multiphysical Modelling in OpenFOAM, Riga, 2011.

[31] C. Winter and D. Tartakovsky, *Groundwater flow in heterogeneous composite aquifers*, Water Resour. Res, 38 (2002), pp. 1–11, https://doi.org/10.1029/2001WR000450.

[32] C. Winter, D. Tartakovsky, and A. Guadagnini, *Moment differential equations for flow in highly heterogeneous porous media*, Surveys Geophys., 24 (2003), pp. 81–106, https://doi.org/10.1023/A:1022277418570.

[33] C. L. Winter, A. Guadagnini, D. Nychka, and D. M. Tartakovsky, *Multivariate sensitivity analysis of saturated flow through simulated highly heterogeneous groundwater aquifers*, J. Comput. Phys., 217 (2006), pp. 166–175, https://doi.org/10.1016/j.jcp.2006.01.047.

[34] X. Yue and W. E, *The local microscale problem in the multiscale modeling of strongly heterogeneous media: Effects of boundary conditions and cell size*, J. Comput. Phys., 222 (2007), pp. 556–572, https://doi.org/10.1016/j.jcp.2006.07.034.